Can. J. Remote Sensing, Vol. 35, No. 5, pp. 411–421, 2009

Using SAR images to delineate ocean oil slicks with a texture-classifying neural network algorithm (TCNNA)[1]

Oscar Garcia-Pineda, Beate Zimmer, Matt Howard, William Pichel, Xiaofeng Li, and Ian R. MacDonald

Abstract. Satellite-borne synthetic aperture radar (SAR) data are widely used for detection of hydrocarbon resources, pollution, and oil spills. These applications require recognition of particular spatial patterns in SAR data. We developed a texture-classifying neural network algorithm (TCNNA), which processes SAR data from a wide selection of beam modes, to extract these patterns from SAR imagery in a semisupervised procedure. Our approach uses a combination of edge-detection filters, descriptors of texture, collection information (e.g., beam mode), and environmental data, which are processed with a neural network. Examples of pattern extraction for detecting natural oil seeps in the Gulf of Mexico are provided. The TCNNA was successful at extracting targets and rapidly interpreting images collected under a wide range of environmental conditions. The results allowed us to evaluate the effects of different environmental conditions on the expressions of oil slicks detected by the SAR data. By processing hundreds of SAR images, we have also found that the optimum wind speed range to study surfactant films is from 3.5 to 7.0 $m \cdot s^{-1}$, and the best incidence angle range for surfactant detection in C-band is from 22° to 40°. Minor postprocessing supervision is required to check TCNNA output. Interpreted images produce binary arrays with imbedded georeference data that are easily stored and manipulated in geographic information system (GIS) data layers.

Résumé. Les données satellite radar à synthèse d'ouverture (RSO) sont utilisées couramment pour la détection des ressources en hydrocarbures, de la pollution et des déversements d'hydrocarbures. Ces applications sont basées sur la reconnaissance de patrons spatiaux particuliers dans les données RSO. On a développé un algorithme de classification de texture basé sur les réseaux de neurones, l'algorithme TCNNA, qui permet de traiter les données RSO à partir d'un grand nombre de modes faisceau pour extraire ces patrons des images RSO en s'appuyant sur une procédure semi-dirigée. Notre approche utilise une combinaison de filtres de détection de contours, de descripteurs de texture, d'information sur l 'acquisition (p. ex. mode du faisceau) et de données environnementales, le tout traité dans le contexte d'un réseau de neurones. On présente des exemples d'extraction de patrons pour détecter des suintements naturels de pétrole dans le golfe du Mexique. L'algorithme TCNNA a permis d'extraire des cibles et d'interpréter rapidement des images acquises dans une grande variété de conditions environnementales. Les résultats ont permis d'évaluer les effets des différentes conditions environnementales sur les expressions des nappes d'hydrocarbures détectées avec les données RSO. En traitant des centaines d'images RSO, on a trouvé également que l'intervalle de vent optimal pour étudier les films de surfactants se situe entre 3,5 et 7,0 $m \cdot s^{-1}$ et que le meilleur intervalle d'angle d'incidence dans la bande C pour la détection des surfactants est de 22° à 40°. Une procédure dirigée minimale est nécessaire durant le post-traitement pour valider les extrants de TCNNA. Les images interprétées produisent des

Received 14 January 2009. Accepted 12 November 2009. Published on the Web at http://pubservices.nrc-cnrc.ca/cjrs on 12 April 2010.

O. Garcia-Pineda[2] and I.R. MacDonald. Oceanography Department, Florida State University, 117 N. Woodward Ave., Tallahassee, FL 32306-4320, USA.

B. Zimmer. Department of Mathematics and Statistics, Texas A&M University at Corpus Christi, 6300 Ocean Drive, Corpus Christi, TX 78412, USA.

M. Howard. Department of Oceanography, Texas A&M University, O&M Building, Room 614, College Station, TX 77843, USA.

W. Pichel. Center for Satellite Applications and Research (STAR), National Environmental Satellite, Data, and Information Service (NESDIS), National Oceanic and Atmospheric Administration (NOAA), Camp Springs, MD 20746, USA.

X. Li. IM Systems Group, NESDIS, NOAA, Room 102, NOAA Science Center, Camp Springs, MD 20746, USA.

[1]This report was prepared as an account of work sponsored by an agency of the US Government. Neither the US Government nor any agency thereof, nor any of their employees, makes any warranty, express or implied, or assumes any legal liability or responsibility for the accuracy, completeness, or usefulness of any information, apparatus, product, or process disclosed, or represents that its use would not infringe privately owned rights. Reference herein to any specific commercial product, process or service by trade name, trademark, manufacturer, or otherwise does not necessarily constitute or imply its endorsement, recommendation, or favoring by the US Government or any agency thereof. The views and opinions of authors expressed herein do not necessarily state or reflect those of the US Government or any agency thereof.

[2]Corresponding author (e-mail: oscar.oggp@gmail.com).

configurations binaires avec des données géoréférencées intégrées qui peuvent être facilement stockées et manipulées dans les couches d'un système d'information géographique (SIG).
[Traduit par la Rédaction]

Introduction

The ability of synthetic aperture radar (SAR) to detect features of the ocean's surface depends on the interactions between the SAR pulse of microwave energy and the sea surface. The radar return from varying roughness of the surface capillary and short gravity waves produces unique patterns in the radar imagery (Holt and Hilland, 2000). SAR is therefore useful for detecting surfactant layers produced by floating oil. Ocean slicks are a subset of ocean features detected in SAR data. They are areas of distinctly contrasting brightness against the radar backscatter produced by wind-generated ripples. Slicks are contiguous areas in which Bragg scattering at a wavelength scale of ~0.01–0.10 m is suppressed by layers of oil (Alpers and Espedal, 2004; Hu et al., 2008), biological surfactants, or floating vegetation (Huehnerfuss et al., 1983). The application of Bragg scattering theory for ocean imaging has been reviewed (Holt, 2004; Thompson, 2004). As shown in **Figure 1**, the SAR return from the ocean surface depends on the wavelength of small surface waves (0.7–10.0 cm), the radar electromagnetic wavelength (λ_r), and the incidence angle (θ) of the radar energy. When sea surface capillary waves are damped by viscoelastic properties of a thin layer of hydrocarbons (~0.1 µm), a larger proportion of radar energy is reflected away from the satellite's detector. Hydrocarbons on the sea surface then can be interpreted as radar-dark regions in SAR images. The persistence of surfactant layers is affected by processes like evaporation, wind, surface currents, photolysis, spreading, flocculation, and dissolution (**Figure 1**).

Oil slicks can emanate from accidental, transient releases of oil from ships or platforms. Under these circumstances, the feature of SAR data will reflect the presence of the source and (or) dispersion history following the release event. In contrast, oil slicks from natural seeps are perennial features, usually relatively small in volume, that are confined to discrete geographic areas (MacDonald et al., 2002). Natural seeps are abundant in the Gulf of Mexico and in other coastal margins worldwide (Kvenvolden et al., 1992). The locations of many active seeps have been verified by submersible sampling (MacDonald et al., 1996) or inferred from geophysical data (Roberts, 2006). Natural seeps therefore produce repeated effects across a wide area of the Gulf of Mexico and provide an excellent source of ocean slicks in multiple SAR images. Because sensor parameters and environmental conditions vary among SAR images, algorithm results can be tested over a range of possible slicks.

Expressions of the thinnest oil slicks can range in width from 60 m to several hundred metres and are typically several thousand metres in length. The ability of SAR to image natural oil slicks is also strongly influenced by environmental conditions, particularly wind speed and sea state. As described in several studies (De Beukelaer et al., 2003; Espedal and Wahl, 1999; Fortuny-Guasch, 2003; Miranda et al., 2004), biogenic surfactants, pollution, and oil slicks from natural hydrocarbon seepage are detectable in a wind speed range of from 2 to 10 $m \cdot s^{-1}$ and in an angle of incidence range from 20° to 45°. Ocean SAR image interpretation becomes more problematic when ancillary meteorological and oceanographic data are unavailable. Detection of slicks is challenged when wind speeds are too high for surfactant layers to form. Another challenge is false targets that occur when low-wind conditions

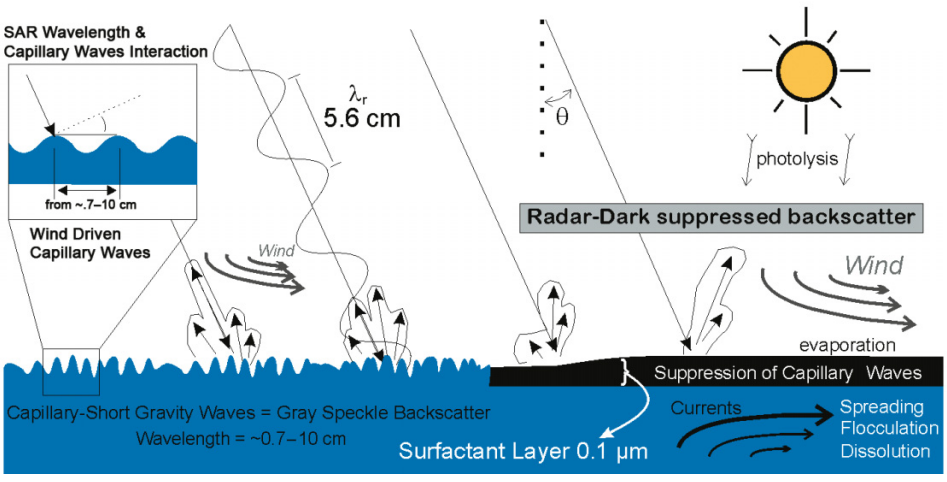

Figure 1. Illustration of the Bragg scattering in the ocean is shown on the left. The radar electromagnetic wavelength is 5.6 cm. The effects of a floating oil (surfactant) layer on radar backscatter are shown on the right, along with oceanographic and atmospheric processes that break down the layer over time.

produce extensive dark areas (low-wind features). In addition, the time required to manually delineate and quantify features of interest constrains the number of images that can be studied, and standard image processing techniques do not fully solve this problem. Brightness thresholding captures numerous false targets; also, standard methods of edge detection do not perform well where intense noise or SAR processing artifacts are present. Automated routines for semisupervised pattern recognition and image segmentation have the potential to improve analysis of the SAR archive for basin-wide and long time-series investigations.

In this paper we therefore describe a texture-classifying neural network algorithm (TCNNA), which analyzes the textural content of SAR data in the context of sensor parameters and environmental variables. The algorithm was developed using verified features (ocean slicks) produced by natural oil seeps in the Gulf of Mexico. However, the general approach may be applicable to other classes of ocean features.

Datasets

Our materials includes SAR images and environmental data. This section is a description of the datasets and preparatory steps towards the image processing.

SAR image achieve

Through data-sharing agreements with the National Aeronautical and Space Administration (NASA) and support from the Alaska Satellite Facility (ASF), a collection of almost 700 RADARSAT-1 images covering the Gulf of Mexico was acquired. This collection comprised a variety of SAR products that differ in resolution, incidence angle, and length of revisit time. Natural oil slicks were visible in many of these images. This collection made it possible to compare oil slicks imaged with different sensor parameters and under different environmental conditions.

A single radar image is usually displayed as an 8-bit (gray-scale) image. Brightness variation and dark features are present, depending on the geophysical effect of surfactants (Espedal and Wahl, 1999). The intensity of each pixel represents the proportion of microwaves backscattered from that area of sea surface. Calm sea surfaces appear dark in SAR images. However, rough sea surfaces may appear bright, especially when the incidence angle is small (Fortuny-Guasch, 2003). Also, in ScanSAR mode, changes in backscatter from one side of an image to the other are a factor of microwave return due to incidence angle.

Quality control of the data required a series of steps. After converting analog SAR signals from RADARSAT-1 to binary SAR data, the ASF Data Center provided the SAR data in Committee on Earth Observation Satellites (CEOS) level one SKY telemetry format (Gens and Logan, 2003). Converter tool software provided by ASF was then used to construct GeoTIFF images from the raw binary SAR data. However, a set of fixed oil platforms was used to verify and fix the georectification. Offsets in the georectification were found from within a single pixel up to 733 pixels.

Environmental data

In our initial evaluation (Garcia-Pineda et al., 2008), we examined a variety of environmental factors to determine how they influenced performance of the TCNNA for detecting oil slicks. These variables included sea surface temperature (SST), sea surface height (SSH), ocean currents, wind conditions at the moment of the SAR snapshot, and wind history up to 9 h before each SAR frame. The data sources included the following: (*i*) National Oceanic and Atmospheric Administration (NOAA) Data Buoy Center (NDBC); (*ii*) Near Real-Time Altimeter Project by Colorado Center for Astrodynamics Research; (*iii*) NOAA CoastWatch; and (*iv*) Wind Port Model, provided by Texas A&M University (http://seawater.tamu.edu/tglo/rxindex.html).

All of the aforementioned variables potentially affect development of surfactant layers over natural seeps; however, careful review showed that prevailing wind conditions during SAR data collection was the most significant variable, i.e., inclusion of other variables resulted in no or minimal improvement in algorithm performance (Garcia-Pineda et al., 2008). SAR measures backscattering energy, normalized radar cross section (NRCS) from the ocean surface (Valenzuela, 1978). Various geophysical model functions (GMFs) have been developed to derive ocean surface wind speed and direction from the backscatter signal. For C-band radar, i.e., RADARSAT SAR or Environmental Satellite Advanced Synthetic Aperture Radar (ENVISAT ASAR), at moderate incidence angles (20°–45°), some of the most widely used GMFs for converting backscatter signal to ocean surface wind are CMOD4 (Stoffelen and Anderson, 1997), CMOD5 (Hersbach, 2005), and CMOD_IFR2 (Quilfen et al., 1998). To minimize speckle noise, the NRCSs are averaged over a few neighboring pixels. The final wind product usually has a lower resolution than that of SAR, but it still provides higher spatial resolution for sub-kilometre wind measurements than any other spaceborne sensor can achieve.

Since SAR has only one viewing angle at a location or pixel, wind speed and direction cannot simultaneously be derived using the CMOD models. Therefore, to derive sea surface wind speed, we must find wind direction first. The wind direction is obtained from the US Navy Operational Global Atmospheric Prediction System (NOGAPS) model. The NOGAPS wind direction output was selected for the closest match to SAR image acquisition time. The NOGAPS output for each grid point (defined as 1° latitude by 1° longitude) is interpolated to estimate wind directions over the SAR image. We then apply CMOD5 GMFs to derive wind speeds used for further oil spill analysis. The CMOD5-derived wind products are very well validated, with a standard deviation of about 2 $m \cdot s^{-1}$, when compared with buoy and QuikSCAT data (Monaldo et al., 2001; 2004)

Analyses

The goal of the TCNNA is to segment an original SAR scene into a binary image so that each pixel is classified as feature or nonfeature. To achieve this, we constructed an input layer vector (ILV) of conditions for each pixel. The ILV contains data and conditions ordered as follows: (*i*) radar backscatter detected by satellite, represented by the eight-bit pixel value; (*ii*) radar incidence angle; (*iii*) wind speed and direction; (*iv*) pixel neighborhood descriptors; and (*v*) convolution of a series of texton filters (described in the next section) over a regular neighborhood centered on the pixel (**Figure 2**). Available wind model resolution is different from that of SAR images. To match data spatially, input values for wind were computed based on linear interpolation from pixel locations and model outputs.

Pixel neighborhood texture descriptors

The first step toward feature segmentation in SAR imagery is to evaluate the size of features under analysis and SAR spatial resolution. In **Figure 3**, ScanSAR narrow beam mode (collected on 21 July 1998), ScanSAR wide beam mode (collected on 9 June 1999), and standard beam mode 1 (collected on 20 May 2006) from RADARSAT-1 are shown, covering different extents in the Gulf of Mexico where oil slicks from natural hydrocarbon seepage occur. Previous work has shown that natural oil slicks in the Gulf of Mexico range in width from a few tens of metres to as much as 500 m. Because the pixel sizes for different SAR modes (using data with resampled spatial resolution) range from 6.25 m to 50 m, the TCNNA must be scaled to recognize slicks over a range of sizes, irrespective of sensor resolution. In this case, oil slick signatures vary in width, and different SAR beam modes have greater or lesser spatial resolution. To ensure detection of narrow slicks, we adjusted the neighborhood size according to the spatial resolution of SAR data. A 25 × 25 pixel neighborhood was used for 12.5 m resolution, a 13 × 13 pixel neighborhood for 25 m resolution, and a 7 × 7 pixel neighborhood for 50 m resolution. With this approach, the input SAR images to the TCNNA can range from standard fine beam mode to wide beam mode.

To standardize comparison between a pixel and its neighborhood, we analyzed the statistical properties of the neighborhood of each pixel using texture descriptors (Gonzalez et al., 2004), i.e., mean, standard deviation, smoothness, third moment, uniformity, and entropy. These values are included with the ILV, and its kernel size is adapted depending on SAR resolution. This analysis was important because the texture of SAR images varies within different regions of an image depending on radar incidence angle and local sea state. The next level of analysis detected features using texture filters, namely the Leung–Malik filter bank (LMFB) (Leung and Malik, 2001). For oil slick detection, only edge and bar detectors were used (the first 36 filters of the 48 element LMFB filter set). For image segmentation, representation of textures

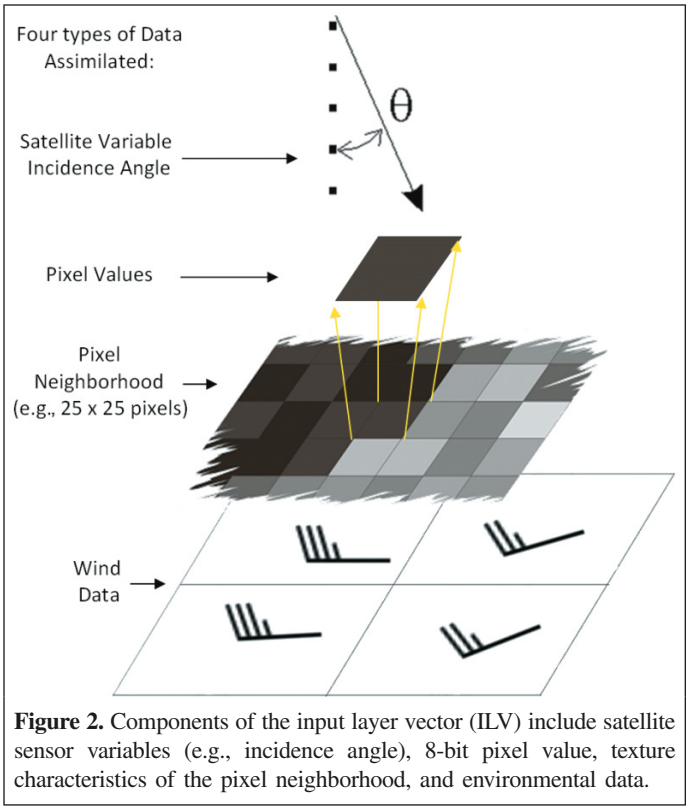

Figure 2. Components of the input layer vector (ILV) include satellite sensor variables (e.g., incidence angle), 8-bit pixel value, texture characteristics of the pixel neighborhood, and environmental data.

using filter responses is extremely versatile. The filters are rescaled to the same dimensions as those of the texture neighborhood. Each pixel and its texture neighborhood are then convolved with each of the 36 LMFB filters as outlined below.

For each pixel of the image matrix, each of the filter matrices is matched to the appropriate neighborhood of surrounding pixels. Convolution multiplies all matching filter and image pixels and sums the results. The process is repeated for each of the 36 LMFB filters. Each image consists of a matrix of pixels, and $\mathbf{Z}(i, j)$ denotes the measurement at the (i, j) pixel. The LMFB is used for convolution with the image matrix and then detects if the image contains an edge or a bar associated with a slick. The mirror image of each LMFB matrix is laid over a region of the large image matrix, and matching terms are multiplied together and then all added up. Let **A** denote an $m \times m$ matrix, and then the value $C(i, j)$ of the convolution of the filter matrix **A** with the image matrix **Z** is defined pixel by pixel as

$$C(i,j) = \sum_{k_2=1}^{m}\sum_{k_1=1}^{m} \mathbf{A}(k_1,k_2)\mathbf{Z}\left(i+\left\lceil\frac{M}{2}\right\rceil-k_1, j+\left\lceil\frac{M}{2}\right\rceil-k_2\right)$$

The results of the 36 convolutions with the LMFB become part of the ILV for each pixel.

Input layer vector

As a result of the processing steps described above, each pixel has an associated ILV that contains a set of values. These values are the following: pixel value, incidence angle, wind

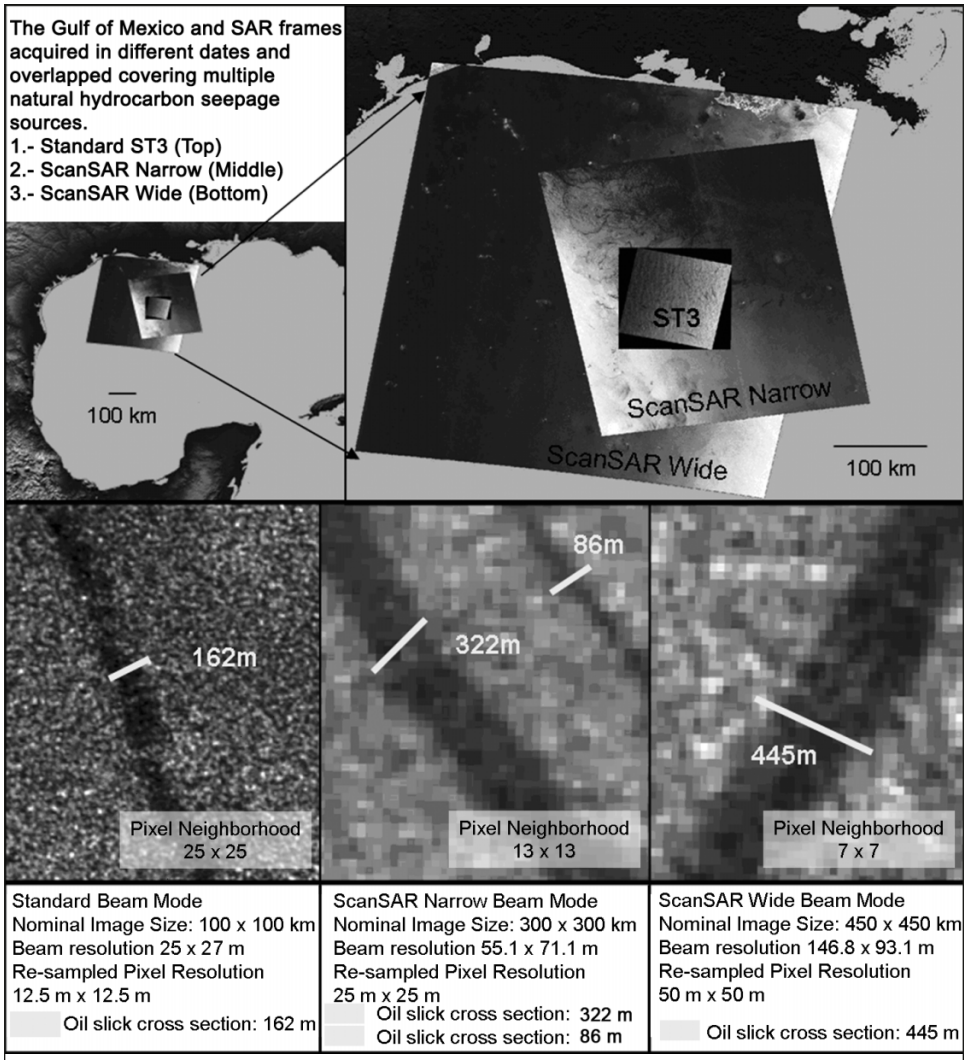

Figure 3. The relationship between the size of the features (in this case oil slicks) and the spatial resolution of the different beam modes is critical for defining the appropriate size of pixel neighborhood to detect boundaries. The upper panel shows coverage comparison of three SAR beam modes, and the lower panel shows different oil slicks imaged at the resulting three levels of resolution and selection of corresponding pixel neighborhoods.

model output, and neighborhood texture (descriptors and filter convolutions), which are assimilated in a 46-dimensional ILV (**Figure 4**). The goal of the TCNNA is to reproduce, pixel by pixel, classifications a human analyst would make, deciding if a given group of pixels belongs to a feature. In this case, the features are oil-covered water versus clean sea. The TCNNA is trained by applying the ILV to images that were previously classified by human analysts.

Training set

From the image collection archive, a set of 14 images was initially selected for building a training set. The selection was determined considering conditions under which oil slicks from natural hydrocarbon seepage are normally observed in SAR images over the Gulf of Mexico. Human classification of images in the training set proceeded by systematically exploring each image at high magnification. Several images contained no visible oil slicks, others included many large and distinct slicks, and others included a few and indistinct slicks. A majority of the total area of each image was devoid of slicks. The operator would select between 200 and 300 points, distributed more or less evenly over the entire image. If slicks were present, several points were selected within each slick, and several nonslick points were selected adjacent to the slick. Locations were saved in a database containing image name, pixel coordinates, and classification as "slick" or "nonslick" with corresponding values of 1 and 0. Consequently, an ILV was constructed for each pixel in the training set, resulting in a database of 3477 vectors with 46 inputs and one target classification as a value of 1 or 0 (**Figure 4**). The neural net algorithm was trained on this dataset, and several hundred images were processed with the trained algorithm.

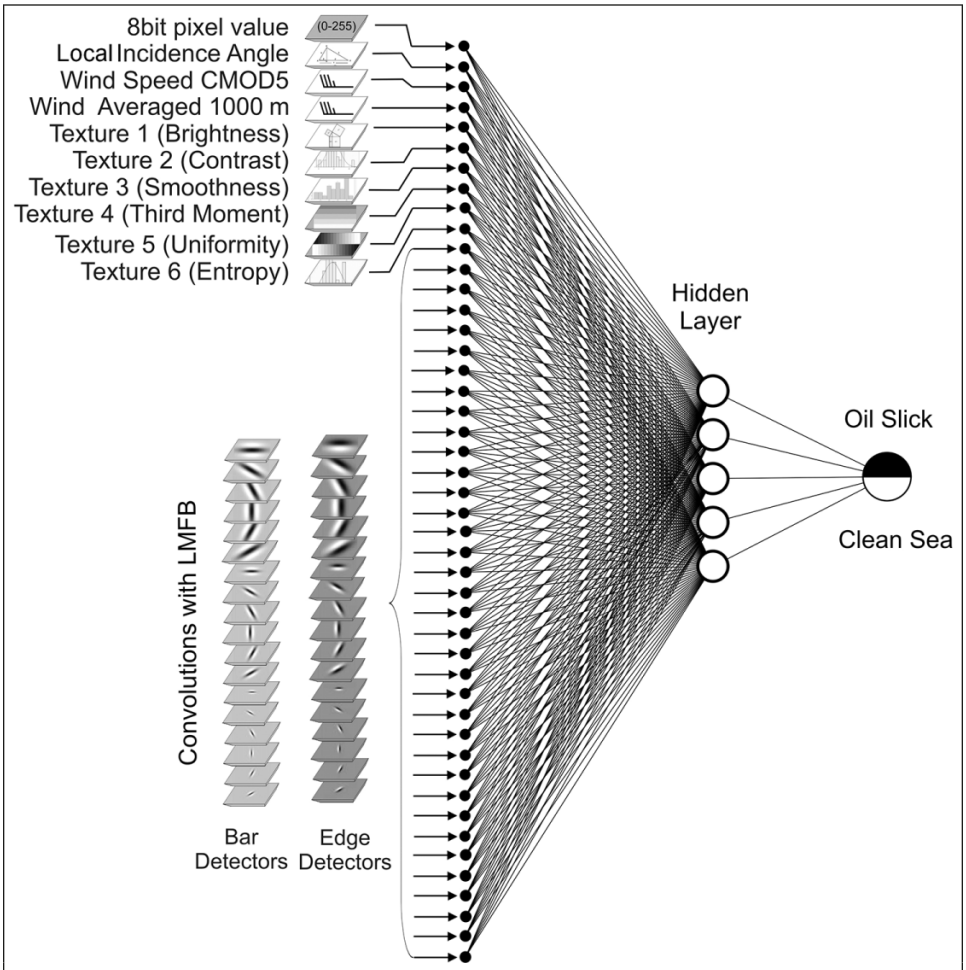

Figure 4. Texture-classifying neural network algorithm (TCNNA). The input layer vector (ILV) comprises 46 variables compiled for each pixel in the SAR image for the neural network classification. For each pixel location in a SAR image, the ILV is made from pixel value, local incidence angle, interpolation of closest wind measurements, six texture descriptors of the neighbor (25 × 25 pixels), and filter reactions to convolutions with the LMFB. Variables were resolved at a unit scale for pixel value and incidence angle, at a spatial scale of 1000 m for environmental variables, and at the pixel neighborhood (kernel) sizes shown in **Figure 2** for texture filters 1–6 and LMFB. Texture variables were computed based on Gonzalez et al. (2004).

In addition to the first training set, a second training set was constructed from 10 different images to test more challenging decision conditions. The goal of this second effort was to discriminate extensive dark areas generated by low-wind features. To achieve this classification, the two wind input values (from the Wind Port Model output interpolations) were substituted into the ILV. The two new inputs consisted of corresponding raw wind data from CMOD5 output and the averaged wind neighborhood of 1000 m around the given pixel from the same CMOD5 as shown in **Figure 4**, the third and fourth inputs from the top. This training set consisted of 5556 pixels, of which 1811 represented oil slicks, 1225 represented low-wind features, and 2520 represented clean sea. The low-wind pixels and the clean-sea pixels were assigned a nonslick value. Further development of the TCNNA and related routines is intended to be an open-source process.[3]

Neural net algorithm

The algorithm designed consists of a pixel-by-pixel, feed-forward neural network (FFNN) classification method. This FFNN has 46 inputs and computes one value to identify each pixel as slick or nonslick as shown in **Figure 4**. We used a two-layer network. The logarithm-sigmoid transfer function was picked because its output range (0–1) allows us to investigate various thresholds to determine the best level of classification. The hidden layer has five neurons. This number was chosen after analyzing and balancing computation time versus increased accuracy.

[3] To promote collaborative research, code and training sets are being made available at www.sarsea.org.

Using the training-set database, a training function that updates weights and bias values according to Levenberg–Marquardt optimization was chosen from the Matlab Neural Network toolbox to update the FFNN. During each training session, the learning process was stopped after approximately 45 epochs when it reached a performance goal of 0.01 mean squared error (MSE).

Each image is an eight-bit file with ~10^8 pixels. For ease in processing, images were tiled in 10 × 10 blocks with a slight overlap to obtain valid convolutions at the edges. The TCNNA processes pixel by pixel in ~10^6 pixel blocks, allocating in memory only information used to process a given pixel and generating the 46-dimensional ILV one pixel at a time.

In the final segmentation process, adaptative thresholding was used depending on backscatter changes that result from changing incidence angle. The threshold associated with each pixel is given by a cosine function of the incidence angle for each pixel.

Results

Validation

Two validation sets were constructed to assess the accuracy of the TCNNA. For the first validation set, a database of 775 ILVs was generated from five different RADARSAT-1 images containing 431 pixels of oil slicks and 344 pixels of clean sea. For the second validation set, a database with 1915 pixels was chosen from five different RADARSAT-1 images containing low-wind features and oil slicks. This second validation set used 552 pixels corresponding to oil slicks, 557 corresponding to low-wind features, and 806 corresponding to clean sea. A validation test was performed using the weights and biases computed by the TCNNA. The overall accuracy classifying the two validation test sets was 98.22% and 97.74% (**Table 1**).

TCNNA versus small incidence angles

The TCNNA worked effectively in RADARSAT-1 images containing oil slicks in low and high incidence angles (**Figure 5**). The fuzzy boundaries produced by low and high incidence angles make discrimination difficult for the human eye. The challenge of discriminating oil pixels in SAR images with high and low incidence angles is shown in **Figure 5**. The TCNNA distinguishes the slick from the nonslick areas of the entire image despite a low contrast difference between target and background and a wide range of image brightness. **Figures 5B**, **5D**, and **5F** and **Figures 5C**, **5E**, and **5G** show the projection from raw image to binary output for slicks in high contrast and low contrast, respectively.

TCNNA versus human classification

Comparison of classifications by a human analyst (**Figures 6A**, **6B**) with TCNNA classifications (**Figures 6C**, **6D**) shows important differences. First, the TCNNA output required much less time to obtain than the manual classification (65 min versus 7.5 h). Second, the human analyst tended to overselect pixels as slick when the boundaries between slick and nonslick were fuzzy. Conversely, the human analyst underselected darker pixels as slicks compared to the performance of the TCNNA (**Figure 6E**). Overall, in the entire image, the human analyst selected slicks equaling 75% of the TCNNA classifications.

Discussion

Neural network algorithms have been developed by other investigators for SAR image analysis to detect floating hydrocarbons (Ramalho and Medeiros, 2007; Topouzelis et al., 2008). Ramalho and Medeiros (2007) developed feature-recognition routines for detecting oil spills. Topouzelis et al. (2008) have used pixel-by-pixel routines to delineate areas of oil-covered water within selected subsets of SAR images. In both cases, the operators strongly suspected the presence of floating oil within the image areas that they analyzed. The TCNNA routines described in this paper used a pixel-by-pixel approach applied to entire SAR images collected in the Gulf of Mexico offshore.

Development of the TCNNA was facilitated by focusing on floating oil released by natural seeps. Because natural seeps are common in the Gulf of Mexico, it was possible to acquire repeat observations of floating oil that occurred under a range of environmental conditions. Synoptic data were available from meteorological buoys, satellite observations, and wind models. Additional data on wind were also extracted from the SAR images using CMOD5 routines (Hersbach, 2005).

As has been noted by several studies, wind has a strong effect on the ability of SAR to detect floating oil (Espedal and Wahl, 1999; MacDonald et al., 2002; Miranda et al., 2004). In earlier work, we found that environmental variables including sea surface height and sea surface temperature contributed little to the performance of the TCNNA (Garcia-Pineda et al., 2008). Consistent with the previous work of other authors, we confirmed the influence of wind on SAR detection of floating oil. However, because we had multiple images over areas

Table 1. Validation test results.

	Oil-slick pixels		Clean-sea pixels		Low-wind pixels		Overall
Validation set	Total	Accuracy (%)	Total	Accuracy (%)	Total	Accuracy (%)	accuracy (%)
1	431	97.02	344	98.25			98.22
2	552	96.55	806	98.07	557	98.60	97.74

Note: Validation set 1 includes Wind Port Model inputs, and validation set 2 includes low-wind features and CMOD5 wind inputs.

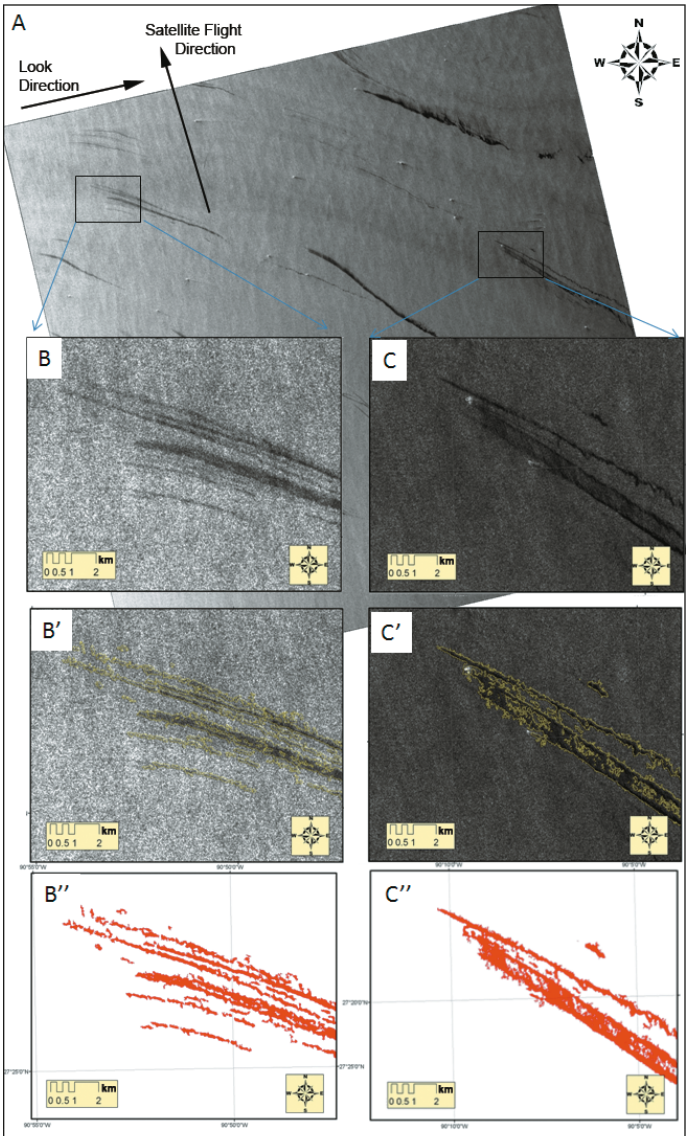

Figure 5. In scenarios where the oil slick classification would be very difficult to perform manually, TCNNA efficiently identifies boundaries between oil slicks and clean sea. (A) Georectified eight-bit SAR image. Incidence angle increases from left to right. (B–B′′) and (C–C′′) show the segmentation of the image from TCNNA processing and output of a binary slick (in red) and nonslick image (in white).

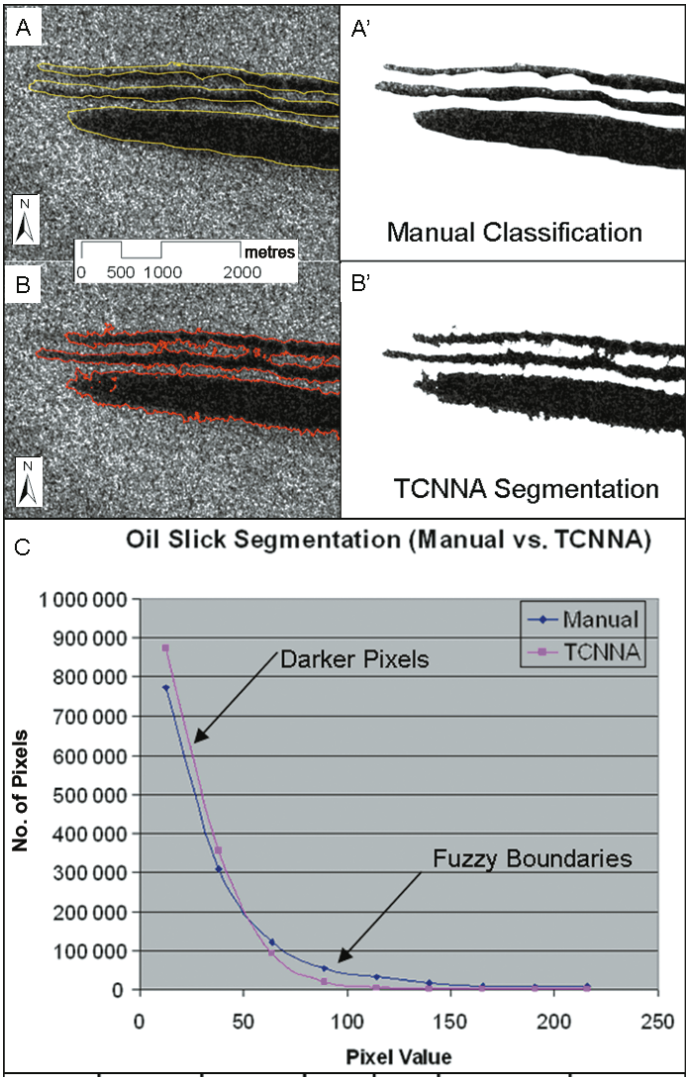

	Mean	Std Dev	Max.	Min.	Total Pixels	Area
Manual	36.9563	49.4843	254	0	1 172 929	183.27 km^2
TCNNA	30.6748	46.6957	254	0	1 194 703	186.67 km^2

Figure 6. Comparison of a manually classified image subset versus TCNNA segmentation (A and B) shows how manual classification can misplace and overlook some boundaries of oil slicks. (C) Manual classification bias depends on pixel values and boundary types.

known to contain natural seeps that extend over many years of observation and we had synoptic environmental data for the collection times, the development of the TCNNA could be used to better constrain the effect of wind on the ability of SAR to detect floating oil. Using ground-truth data from NDBC buoys and from onboard meteorological measurements during cruise expeditions, we observed that in the wind speed range of 3–7 m·s^{-1}, RADARSAT SAR images in the standard and ScanSAR beam modes consistently showed floating oil. Within this range, having wind data, whether from in situ measurement or CMOD5 processing, contributed relatively little to the performance of the TCNNA. This means that the TCNNA can potentially be used for images where no environmental data are available and (or) CMOD5 processing is not possible. Running the TCNNA without wind data greatly streamlines the image-analysis process.

When wind speeds are below about 3 m·s^{-1}, so-called low-wind effects begin to degrade the ability to distinguish oil from large dark areas that occur where the wind is insufficient to generate backscatter. Under these conditions, adding wind data to the ILV significantly improves the way TCNNA discriminates between oil and false targets generated by low-wind regions. The decision of whether or not to add wind to the ILV can be made based on visual inspection of the image. Decision-tree analysis indicates that inclusion of wind variables is helpful. This provides a deterministic criterion for

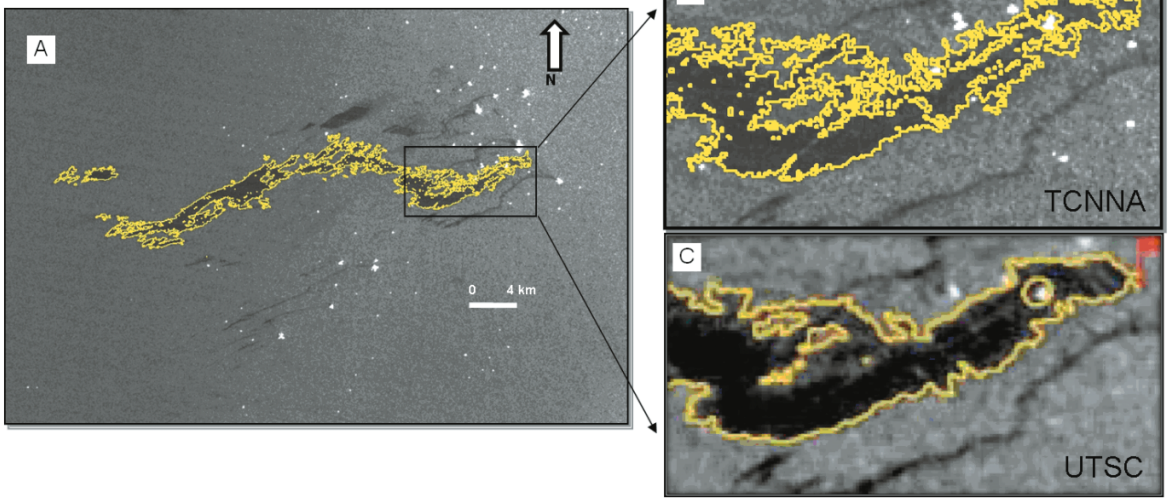

Figure 7. (A) Subset of a RADARSAT-1 image acquired over Mexican oil production field Cantarell where natural hydrocarbon seepage and pollution are detected by TCNNA. (B) Zoom in of the oil slick segmentation processed by TCNNA. The same image has been processed by Pellon et al. (2004) as shown in (C). Both algorithms accurately segmented the area covered by oil. TCNNA area segmentation (65.33 km^2) is more conservative than USTC segmentation (96.10 km^2).

adding wind data to the ILV. Separate training sets are required for running the TCNNA with or without wind data inputs.

Visual inspection of images can also determine when high-wind conditions have degraded the oil-detection capability of SAR. However, in our experience, this determination is less conclusive than that for low-wind conditions. Seasonal variability in average wind speed can be used to screen images; SAR collections during winter months are less likely to support oil detection because of the stronger seasonal winds. Further research on the image characteristics associated with high-wind conditions may produce methods for evaluating whether the wind conditions in an arbitrary image are conducive to oil slick detection. At present, if it is uncertain whether the absence of oil results from lack of oil or unfavorable wind, then wind data from buoys or CMOD5 processing are required.

Results of the TCNNA can provide precise estimates for the total extent of floating oil. The pixel-by-pixel output generates polygons that are much more detailed than could reasonably be produced by a human operator (**Figures 5** and **6**). Other automated routines applied to oil releases in the Gulf of Mexico have also produced accurate segmentations of oil-covered water (Miranda et al., 2004). Comparing the TCNNA output with the results given by the semivariogram classifier described in Pellon et al. (2004) illustrates the difference between the two products (**Figure 7**). Both accurately show the extent of the oil slick. However, one difference is that TCNNA estimates of the total area covered by oil are significantly more conservative than the semivariogram results, probably because of the pixel-by-pixel processing of the TCNNA. This difference would be important for estimating the total quantities of oil present or variations in the flux from natural sources because the two approaches would produce different estimates.

An advantage of this algorithm is that it can process either the whole image or a region of interest for the user. The threshold is automatically adjusted based on the incidence angle. The output is a binary GeoTIFF image (about 1 Mb) containing polygons representing oil slick areas and retaining geospatial registration for easy handling and generation of spatial statistics in mapping software. In addition, this algorithm exports results in a standard geographic information system (GIS) layer for maps (shape files) with polygons containing attributes like sea surface area, SAR image identification collection, and the date.

Conclusions

The reliability of the texture-classifying neural network algorithm (TCNNA) was assessed after processing several hundred images containing oil slicks under different scenarios, including cases where the edges of slicks were indistinct and difficult to classify visually. The TCNNA produces results that match or exceed what can be done by human analyst and in a fraction of the time needed for manual classification.

TCNNA results allow us to evaluate effects of different environmental conditions on expressions of oil slicks detected by synthetic aperture radar (SAR) satellites. In combination with a large archive of SAR images over the Gulf of Mexico, TCNNA also will allow characterization of a multiyear process like flux variation of a natural hydrocarbon seepage source and estimation of the entire Gulf of Mexico contribution of hydrocarbon transfer from the ocean to the atmosphere. Other processes may be detected with the TCNNA if suitable training sets are obtained. Among other processes that can be analyzed using TCNNA are oil spills, coastal upwelling, and patterns in

sargassum, like the magnitude and distribution of floating sargassum (algal) mats.

Acknowledgments

This research has been supported by the Minerals Management Service contract 1435-01-05-39187. We want to acknowledge the generous support of Rebecca Sanches and ASF staff for their invaluable collaborations in this research. Thanks to Karen Bannerman from MDA Geospatial Services for the valuable collaboration. Thanks to CONACYT Mexico for the invaluable support. We want also to acknowledge the US Department of Energy (DOE) Natural Energy Technology Laboratory (DOE contract DE-NT 0005638). The views, opinions, and findings contained in this report are those of the authors and should not be construed as an official National Oceanic and Atmospheric Administration or US Government position, policy, or decision.

References

Alpers, W., and Espedal, H. 2004. Oils and surfactants. In *Synthetic aperture radar marine user's manual*. Edited by C.R. Jackson and J.R. Apel. US Department of Commerce, Washington, D.C. pp. 263–277.

De Beukelaer, S.M., MacDonald, I., Guinnasso, N.L.J., and Murray, J.A. 2003. Distinct side-scan sonar, RADARSAT SAR, and acoustic profiler signatures of gas and oil seeps on the Gulf of Mexico slope. *Geo-Marine Letters*, Vol. 23, pp. 177–186.

Espedal, H., and Wahl, T. 1999. Satellite SAR oil spill detection using wind history information. *International Journal of Remote Sensing*, Vol. 20, No. 1, pp. 49–65.

Fortuny-Guasch, J. 2003. Improved oil slick detection and classification with polarimetric SAR. In *Applications of SAR Polarimetry and Polarimetric Interferometry: Proceedings of the Workshop on POLinSAR*, 14–16 January 2003, Frascati, Italy. Edited by H. Lacoste. ESA Publications Division, ESTEC, Noordwijk, The Netherlands. SP-529.

Garcia-Pineda, O., MacDonald, I.R., and Zimmer, B. 2008. Synthetic aperture radar image processing using the supervised textural–neural network classification algorithm. In *IGARSS'08, Proceedings of the International Geoscience and Remote Sensing Symposium*, 7–11 July 2008, Boston, Mass. IEEE, New York. Vol. 4, No. 4, pp. 1265–1268.

Gens, R., and Logan, T. 2003. *Alaska Satellite Facility software tools*. Geophysical Institute, University of Alaska, Fairbanks, Alaska.

Gonzalez, R., Woods, R., and Eddins, S. 2004. *Digital image processing using Matlab*. Pearson Education, Inc., Upper Saddle River, N.J. 609 pp.

Hersbach, H. 2005. *CMOD5: An improved geophysical model function for ERS C-band scatterometry*. European Centre for Medium Range Weather Forecasting (ECMWF), Reading, U.K. Technical Memorandum 395, pp. 1–50.

Holt, B. 2004. SAR imaging of the ocean surface. In *Synthetic aperture radar marine user's manual*. Edited by C.R. Jackson and J.R. Apel. US Department of Commerce, Washington, D.C. pp. 25–80.

Holt, B., and Hilland, J. 2000. Rapid-repeat SAR imaging of the ocean surface: are daily observations possible? *Johns Hopkins APL Technical Digest*, Vol. 21, No. 1, pp. 162–169.

Hu, C., Li, X., Pichel, W., and Muller-Karger, F. 2008. Detection of natural oil slicks in the NW Gulf of Mexico using MODIS imagery. *Geophysical Research Letters*, Vol. 36, No. 1, pp. 1819–1836.

Huehnerfuss, H., Alpers, W., Garrett, W., Lange, P., and Stolte, S. 1983. Attenuation of capillary and gravity waves at sea by monomolecular organic surface films. *Journal of Geophysical Research*, Vol. 88, pp. 9809–9816.

Kvenvolden, K.A., Ginsburg, G., and Soloviev, V. 1992. Worldwide distribution of subaquatic gas hydrates *Geo-Marine Letters*, Vol. 13, No. 1, pp. 32–40.

Leung, T., and Malik, J. 2001. Representing and recognizing the visual appearance of materials using three-dimensional textons. *International Journal of Computer Vision*, Vol. 43, No. 1, pp. 29–44.

MacDonald, I., Reilly, J., Best, S., Venkataramaiah, R., Guinasso, N., and Amos, J. 1996. Remote sensing inventory of active oil seeps and chemosynthetic communities in the northern Gulf of Mexico. In *Hydrocarbon migration and its near-surface expression*. Edited by D. Schumacher and M.A. Abrams. American Association of Petroleum Geologists (AAPG), Tulsa, Okla. AAPG Memoir 66, pp. 27–37.

MacDonald, I.R., Leifer, I., Sassen, R., Stine, P., Mitchell, R., and Guinasso, N. 2002. Transfer of hydrocarbons from natural seeps to the water column and atmosphere. *Geofluids*, Vol. 2, No. 2, pp. 95–107.

Miranda, F.P., Marmol, A.M.Q., Pedroso, E.C., Beisl, C.H., Welgan, P., and Morales, L.M. 2004. Analysis of RADARSAT-1 data for offshore monitoring activities in the Cantarell Complex, Gulf of Mexico, using the unsupervised semivariogram textural classifier (UTSC). *Canadian Journal of Remote Sensing*, Vol. 30, No. 3, pp. 424–436.

Monaldo, F., Thompson, D., Beal, R., Pichel, W., and Clemente-Colon, P. 2001. Comparison of SAR-derived wind speeds with model predictions and ocean buoy measurements. *IEEE Transactions on Geoscience and Remote Sensing*, Vol. 39, pp. 2587–2600.

Monaldo, F., Thompson, D., Pichel, W., and Clemente-Colon, P. 2004. A systematic comparison of QuickSCAT and SAR ocean surface wind speeds. *IEEE Transactions on Geoscience and Remote Sensing*, Vol. 42, pp. 283–291.

Quilfen, Y., Chapron, B., Elfouhaily, T., Katsaros, K., and Tournadre, J. 1998. Observation of tropical cyclones by high-resolution scatterometry. *Journal of Geophysical Research*, Vol. 103, No. C4, pp. 7767–7786.

Ramalho, G., and Medeiros, F. 2007. Improving reliability of oil spill detection systems using boosting for high-level feature selection. In *Image Analysis and Recognition: Proceedings of the 4th International Conference*, 22–24 August 2007, Montréal, Que. Edited by M. Kamel and A. Campilho. Springer, Berlin. pp. 1172–1181.

Roberts, H. 2006. Seafloor reflectivity. An important seismic property for interpreting fluid/gas expulsion geology and the presence of gas hydrate. *The Leading Edge*, Vol. 25, pp. 620–628.

Stoffelen, A., and Anderson, D. 1997. Scatterometer data interpretation: Estimation and validation of the transfer function CMOD4. *Journal of Geophysical Research*, Vol. 102, pp. 5767–5780.

Thompson, D.R. 2004. Microwave scattering from the sea. In *Synthetic aperture radar marine user's manual*. Edited by C.R. Jackson and J.R. Apel. US Department of Commerce, Washington, D.C. pp. 117–138.

Topouzelis, K., Karathanassi, V., Pavlakis, P., and Rokos, D. 2008. Dark formation detection using neural networks. *International Journal of Remote Sensing*, Vol. 29, No. 16, pp. 4705–4720.

Valenzuela, G. 1978. Theories for the interaction of electromagnetic and ocean waves — A review. *Boundary-Layer Meteorology Journal*, Vol. 13, pp. 61–85.